Neutron scattering study of thermally excited density fluctuations in a dense classical fluid

T. A. Postol and C. A. Pelizzari
Solid State Science Division, Argonne National Laboratory, Argonne, Illinois 60439
(Received 9 June 1978)

Collective density fluctuations in ^{36}Ar gas at 456 atm pressure and 295 K have been studied by thermal neutron scattering using time-of-flight techniques. Well-defined collective modes are observed for wave-vector transfers $\vec{k} \lesssim 0.1$ Å^{-1} which become strongly damped at larger k. The data have been compared in detail with predictions of the generalized Enskog equation. Although extrapolation of the predictions to $k = 0$ gives the correct transport coefficients to better than 5% accuracy, the generalized Enskog equation does not properly predict the wave-vector dependence of the scattering law.

I. INTRODUCTION

The central aim of inelastic light and coherent neutron scattering experiments on fluids is to provide detailed microscopic information about the dynamical behavior of thermal fluctuations in many-body systems. These experiments, when properly performed and analyzed, can directly measure the spectral distribution of the density-density correlation function over a wide range of wave vectors and frequencies.[1] A principal advantage associated with measuring this time correlation function (TCF) is the fact that its time, wave vector, density, and temperature dependence provide a sensitive measure of microscopic properties which cannot be observed from measurements of transport coefficients.

In recent years, numerous workers have contributed to a general formal theory of TCFs which describes the nonequilibrium behavior of many-body systems in terms of spectral distributions at fixed wave vector.[2] The development of this formal theory has been paralleled by the application of modern many-body techniques which attempt to calculate TCFs at a molecular level.[3] Computer experiments have also been used to numerically calculate TCFs of interest for finite model fluids.[4] The enormous growth in understanding of the microscopic properties of TCFs has opened new and interesting questions which relate to the importance of potential and many-body effects governing their wave-vector and frequency dependence.

The TCF of interest in this paper is the density-density correlation function of argon gas at 456 atm and 295 °K, whose Fourier transform, the dynamic structure factor, we have measured by neutron scattering using a time-of-flight technique. In this region of temperatures and densities, the transport coefficients are well described by a modified version of the Enskog kinetic theory.[5] As we demonstrate below, further modifications are necessary before the Enskog theory can be made to agree with the present experiment. However, recent computer experiments on dense hard-sphere fluids[6] indicate that the Enskog theory quantitatively predicts the behavior of the density-density correlation function at densities well above 0.47 times that of close packing. Comparison of these computer results with experimental data are therefore of some interest.

II. DYNAMIC STRUCTURE FACTOR

A. General considerations

The quantity of interest in inelastic coherent neutron scattering is the dynamic structure factor or scattering law[7]

$$S(\vec{k},\omega) = \frac{1}{2\pi}\int_{-\infty}^{\infty} dt \int d\vec{r}\, e^{i(\vec{k}\cdot\vec{r}-\omega t)} G(\vec{r},t)\,, \tag{2.1}$$

where

$$G(\vec{r},t) = \frac{1}{N}\sum_{i=1}^{N}\sum_{j=1}^{N}\langle \delta(\vec{r} - \vec{R}_i(t) + \vec{R}_j(0))\rangle\,,$$

N is the number of particles in the system, and $\vec{R}_i(t)$ is the coordinate of the ith particle at time t, which is the space-time Fourier transform of the density-density correlation function. The general behavior of this correlation function as a function of frequency at fixed wave vector is well known.[8]

At wave vectors which are small compared to the inverse of a particle mean free path (we will assume a class of systems in which the concept of mean free path is meaningful), the dynamics of the fluid are dominated by collisions. At these wave vectors, the system can be described in terms of a set of dynamical variables which vary slowly in time compared to the mean collision time, and slowly in space compared to a mean free path. In consequence, concepts of continuity and local equilibrium are valid and, if the system is far from the critical point, the dynamics of the

density-density correlation function are governed by the linearized Navier-Stokes equations.

At intermediate wave vectors, that is, at wave vectors which are on the order of an inverse mean free path, the dynamics of the system are controlled by the local structure, short-time free-particle motion and intermediate-time collisions with neighbors. For purposes of discussion, we will call this intermediate-wave-vector regime in which hydrodynamic concepts begin to lose meaning the hydrodynamic to kinetic transition (or simply transition) regime.

At wave vectors which are large compared to an inverse mean free path, particles rarely undergo collisions over distances on the order of $1/k$ and the dynamic structure factor has the free-particle form.

B. Relation to kinetic theory of fluids

One of the principal successes of kinetic theory is that it provides a quantitatively correct description of the dynamic structure factor at both small and large wave vectors and frequencies.[9] This success is traceable, at least in part, to the fact that the kinetic-theory approach contains both the particle coordinates and momenta explicitly. Therefore, the mechanical features of a many-body system are explicitly accounted for.

Of central interest in kinetic theory is the phase-space density function[10]

$$f(\vec{r},\vec{p},t)=\sum_{i=1}^{N}\delta(\vec{r}-\vec{R}_i(t))\delta(\vec{p}-\vec{P}_i(t)), \tag{2.2}$$

where $\vec{R}_i(t)$ and $\vec{P}_i(t)$ are the position and momentum of the ith particle at time t.

The average of this is proportional to the density of particles in phase space at coordinate $\vec{r}$ and momentum $\vec{p}$ and is of interest because measurable TCFs as well as macroscopic fluxes can be constructed from it. The time-dependent density correlation function, of interest in scattering experiments, can be constructed by first calculating the more fundamental phase space TCF

$$S(\vec{r},\vec{p},\vec{r}',\vec{p}',t-t')=\langle\delta f(\vec{r},\vec{p},t)\delta f(\vec{r}',\vec{p}',t')\rangle, \tag{2.3}$$

where

$$\delta f(\vec{r},\vec{p},t)=f(\vec{r},\vec{p},t)-\langle f(\vec{r},\vec{p},t)\rangle$$

and

$$\langle f(\vec{r},\vec{p},t)\rangle=nf_0(p),$$

where n is the density, the brackets $\langle\ \rangle$ indicate an average over an equilibrium ensemble, and $f_0(p)$ is the normalized Maxwellian. By integrating over the momentum variables $\vec{p}$ and $\vec{p}'$ the density correlation function is obtained:

$$G(\vec{r}',t-t')=\frac{1}{n}\int d\vec{p}\int d\vec{p}\,'\,S(\vec{r},\vec{p},\vec{r}',\vec{p}',t-t')$$
$$=\langle n(\vec{r},t)n(0,0)\rangle/n-n. \tag{2.4}$$

The space, time, and momentum dependence of the phase-space correlation function are governed by an exact equation of motion,[10]

$$\frac{\partial S(\vec{r},\vec{p},\vec{p}',t)}{\partial t}+\frac{\vec{p}}{m}\cdot\vec{\nabla}S(\vec{r},\vec{p},\vec{p}',t)$$
$$=\int_0^t dt'\int d^3r'\int d^3p''\phi(\vec{r}-\vec{r}',\vec{p}',\vec{p}'',t-t')$$
$$\times S(\vec{r}',\vec{p}'',\vec{p}',t'). \tag{2.5}$$

The function $\phi(\vec{r},\vec{p},\vec{p}',t)$ is the phase-space memory function, which is in general nonlocal in space and time and contains the effects of the other $N-1$ particles on a given particle.

The spectral distribution of the phase-space correlation function can be constructed from the solution of (2.5). The space-time Fourier-Laplace transform of the phase-space TCF is defined as

$$S(k,\vec{p},\vec{p}',z)=i\int_0^\infty dt\int d\vec{r}\,e^{i(zt-\vec{k}\cdot\vec{r})}$$
$$\times S(\vec{r},\vec{p},\vec{p}',t) \tag{2.6}$$

and is governed by the inital-value equation

$$[z-(\vec{k}\cdot\vec{p})/m]S(\vec{k},\vec{p},\vec{p}',z)$$
$$=\int d\vec{p}''\phi(\vec{k},\vec{p},\vec{p}'',z)S(k,\vec{p}'',\vec{p}',z)+\tilde{S}(\vec{k},\vec{p},\vec{p}'), \tag{2.7}$$

where $\tilde{S}(\vec{k},\vec{p},\vec{p}')$ is the initial value of (2.6), that is, the equal time or equilibrium value of $S(\vec{k},\vec{p},\vec{p}',t)$. $\tilde{S}(\vec{k},\vec{p},\vec{p}')$ has the form

$$\tilde{S}(\vec{k},\vec{p},\vec{p}')=nf_0(p)\delta(\vec{p}-\vec{p}')+n^2h(k)f_0(p)f_0(p'),$$

where

$$h(\vec{k})=\int d^3r[g(\vec{r})-1]e^{i\vec{k}\cdot\vec{r}}$$

and

$$g(\vec{r})=\frac{V}{N^2}\sum_{i\neq j=1}^{N}\langle\delta(\vec{r}-\vec{R}_i(0)+\vec{R}_j(0))\rangle$$

is the static pair distribution function.

The phase-space memory function has two parts, a static time-independent part and a time-dependent many-body (collisional) part:

$$\phi(\vec{k},\vec{p},\vec{p}',z)=\phi^{(s)}(\vec{k},\vec{p},\vec{p}')+\phi^{(c)}(\vec{k},\vec{p},\vec{p}',z),$$

where the unapproximated static part has the form

$$\phi^{(s)}(\vec{k},\vec{p},\vec{p}')=-[(\vec{k}\cdot\vec{p})/m]C(k)f_0(p)$$

with $C(k)$ the direct correlation function

$$C(k)=h(k)/[nh(k)+1] .$$

The spectral distribution of the phase-space correlation function is related to the initial-value solution of (2.7) by

$$S(\vec{k},\vec{p},\vec{p}',\omega)=2\mathrm{Im}[S(\vec{k},\vec{p},\vec{p}',z)]_{z=\omega+i0^+} . \quad (2.8)$$

Comparison of Eq. (2.1) with Eqs. (2.4) and (2.6) shows that $S(\vec{k},\omega)$ is obtained from $S(\vec{k},\vec{p},\vec{p}',\omega)$ by integrating over all values of the momenta $\vec{p}$ and $\vec{p}'$. Thus the quantity measured in a scattering experiment can be directly obtained from kinetic theory. The collisional part of the phase-space memory function is in general extremely complicated and is of central interest in many-body calculations. It has been evaluated at low densities for hard-sphere systems and corresponds to a generalized Enskog theory.[11] This theory predicts the conventional Enskog transport coefficients but does not have the defects of the Enskog equation at short times. The correct short-time behavior of the generalized Enskog equation is a consequence of the proper treatment of the time-independent mean-field part of the memory function $\phi^{(s)}(\vec{k},\vec{p},\vec{p}')$.

C. Calculation using kinetic model

The dynamic structure factor can be numerically obtained from the generalized Enskog equation by applying the method of kinetic models. The procedure is lucidly described in Refs. 12 and 13 and will not be discussed here. The kinetic model used in our analysis is the triple-relaxation-time (QTRT) model of Ref. 13 rather than the single-relaxation-time model of Ref. 12. The reason for this is as follows: The speed of sound and the coupling of the sound and heat modes at small wave vectors are implicitly contained in the memory function. The kinetic-model procedure approximates the memory function in terms of an expansion in an orthogonalized set of momentum variables. The coefficients of this expansion, the matrix elements of the memory function, can be directly related to the thermodynamic and hydrodynamic properties of the kinetic-model solution.[14] The QTRT model includes matrix elements which model the small-k behavior of the memory function to better include viscosity and thermal conductivity effects at the hydrodynamic limit. This reflects itself in a much more accurate numerical representation of the TCF near the hydrodynamic limit. Since some of our data appear close to this limit, the QTRT model is an obvious choice.

A difficulty in using the hard-sphere generalized Enskog equation is that it contains the thermodynamics for hard spheres rather than realistic potentials. In addition, the transport coefficients are sensitive to the choice of a hard-sphere diameter r_0 and the pair correlation function at contact $g(r_0)$. A further complication occurs because the choice of the structure factor $S(k)$ [$=1+nh(k)$] strongly affects both the shape and intensity of the calculated dynamic structure factor. The effects of these variables on numerical calculations of the dynamic structure factor are illustrated in Figs. 1 and 2. In Fig. 1(a) the full numerical solution of the generalized Enskog equation is shown [$k=0.10$ Å^{-1}, $r_0=3.4$ Å, $g(r_0)=1.446$, and $S(k)=0.4223$]. This solution includes the exact static piece of the hard-sphere memory function and an approximate collisional piece of the memory function. The approximate collisional piece of the memory function used is the exact low-density hard-sphere memory function[11] scaled to high densities. This is the Enskog nonlocal collision term which treats collisions as nonlocal uncorrelated events between hard spheres. In Fig. 1(b) the influence of the nonlocal collisions on the form of the spectrum is demonstrated. The $k=0$ limit of the collisional piece of the memory function is used and the static piece of the memory function has been retained. The system appears much

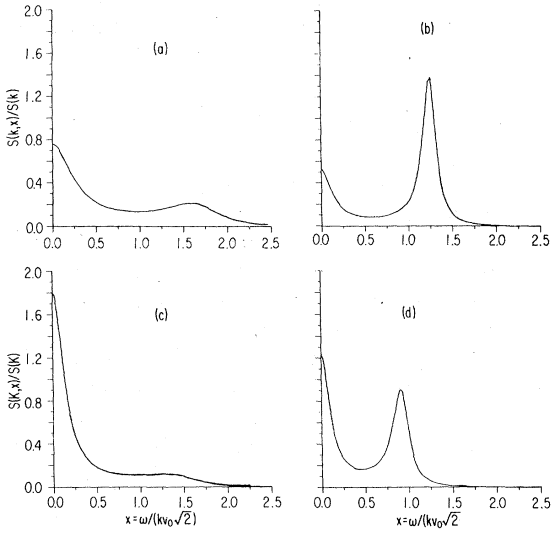

FIG. 1. (a) QTRT model solution of the generalized Enskog equation for a reasonable choice of the parameters r_0 and $g(r_0)$, and the function $S(k)$. (b) Long-wavelength limit of the collisional matrix elements has been used (i.e., fluid effectively composed of "point particles," but retains static structure). (c) Static structure ignored [i.e., $S(k)=1$] but wavelength dependence of matrix elements retained (i.e., fluid composed of finite particles exhibiting no positional correlations). (d) Neither static structure nor finite size of particles included.

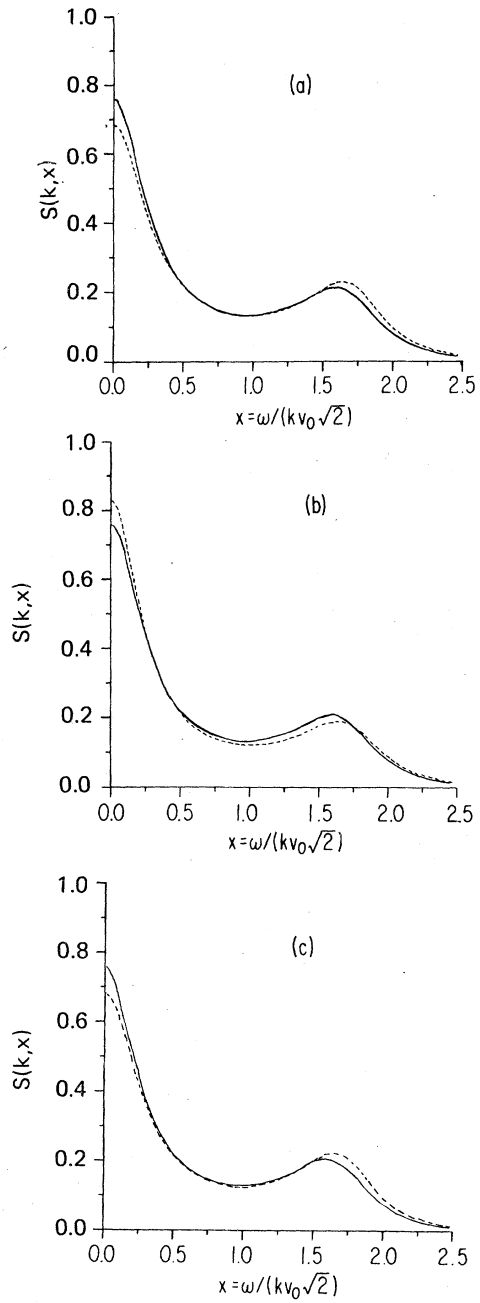

FIG. 2. Sensitivity of the QTRT model solution to 10% changes in the hard-sphere diameter r_0, the pair correlation function at contact $g(r_0)$, and the static structure factor $S(k)$ (see text).

more "plasma" like and the frequency of the collective mode is somewhat smaller. The lower frequency is a consequence of the point-particle treatment of collisions which requires that colliding particles instantly transfer momentum at the same point in space rather than over distances of a hard-sphere diameter r_0. In Fig. 1(c) the Enskog collision term is properly included but the presence of mean-field effects (which are contained in the static piece of the memory function) are neglected by setting $S(k)=1$ [and hence $nC(k)=0$]. In Fig. 1(d) the $k=0$ value of the collision integral is used and the static structure term is not included. This corresponds to the classical Boltzmann limit of the generalized Enskog theory. In Fig. 2 sensitivity of the shape of the power spectrum to the Enskog parameters is shown at $k=0.10$ Å^{-1}. The solid curves in Fig. 2(a), 2(b), and 2(c) show the spectrum which is the best fit to our 0.10-Å^{-1} data arrived at by fixing $r_0=3.4$ Å and fitting for values of $g(r_0)$ and $S(k)$ (see Secs. IV and V). The dashed curve in Fig. 2(a) shows the effect of a 10% smaller value of the hard-sphere diameter r_0. The dashed curve in 2(b) shows the effect of a 10% larger value of $g(r_0)$ and the dashed curve in 2(c) shows the effect of a 10% smaller value of $S(k)$. The result of varying all three parameters is discussed in detail in Sec. V.

III. EXPERIMENT

A. General considerations

The raw data in a time-of-flight inelastic neutron scattering experiment is the scattered intensity at fixed angle as a function of time of arrival after pulsing of the neutron beam. This function is related to the symmetrized dynamic structure factor $S(k,\omega)$ by

$$I(\theta,t)=Na_{\rm coh}^2(k_f/\hbar k_i)\exp(\beta\hbar\omega/2)\times S(k,\omega)\eta(E_f)\,d\Omega\,dE_f\,,$$

where $a_{\rm coh}$ is the coherent scattering length, E_f the final scattered energy equal to $\hbar^2k_f^2/2m$, E_i the incident neutron energy equal to $\hbar^2k_i^2/2m$, $\vec{k}_f,\vec{k}_i$ are the final and incident neutron wave vectors, $k=|\vec{k}_f-\vec{k}_i|$, $\hbar\omega=E_f-E_i$, N is the number of nuclei illuminated by the incident neutron beam, $d\Omega$ the solid angle subtended by the detector, and $\eta(E_f)$ the detector efficiency at the energy E_f. The energy width of a time channel, dE_f, is given by $2E_f dt/t$ where t is the neutron time of flight from sample to detector and dt the time-channel width. It is important to note that dE_f is thus proportional to t^{-3}. This means a Jacobian must be applied to the data before the scattering law is obtained although for modest energy ranges it is not misleading to view time of flight data directly.

The present experiment was performed using the Argonne thermal neutron time-of-flight spectrometer.[15] Spectra were analyzed simultaneously at 15 scattering angles. The scattering angles

TABLE I. Detector configuration used in the present experiment.

Scattering angle	Angular resolution (FWHM)	Solid angle (msr)
± 2.4°	0.30°	0.9
± 3.0°	0.30°	0.9
± 3.6°	0.30°	0.9
± 4.2°	0.30°	0.9
± 4.8°	0.30°	0.9
± 5.4°	0.30°	0.9
± 6.3°	0.60°	1.8
± 7.5°	0.60°	1.8
± 8.7°	0.60°	1.8
11.7°	0.60°	1.8
14.1°	0.60°	1.8
16.5°	0.60°	1.8
18.9°	0.60°	1.8
21.3°	0.60°	1.8
23.7°	0.60°	1.8

ranged from 2.4° to 23.7°, more densely spaced in the small wave-vector-transfer range where the dynamic structure factor was expected to vary most rapidly. At larger wave-vector transfers, angular increments consistent with the anticipated variation of the scattering law in the transition regime were chosen. The detector configuration is summarized in Table I.

In Fig. 3 we show the loci of measurement in the k-ω plane determined by our choice of scattering angles and incident neutron energy. The vertical bar near the origin shows the energy resolution of the spectrometer, which is about 5% of the incident neutron energy. Also shown are dispersion relations for sound excitations (assuming these could exist at large wave vectors) propagating at 500 and 1000 m/sec. As can be seen, the present arrangement is adequate for investigation of excitations with speeds around 500 m/sec, but higher neutron energies are required if stiffer excitations are of interest. In this case maintaining adequate energy and wave-vector-transfer resolution would entail substantial loss of neutron-beam intensity, and such measurements could only be conducted (with suitably designed spectrometers) at high-flux reactors or advanced pulsed neutron sources.

The present measurements utilized the mechanical correlation chopper originated by Sköld[16] to help offset the low counting rate resulting from the smallness of $S(k)$ at small k [for argon at 456 atm, the compressibility limit $S(0) = 0.56$]. Use of the correlation chopper is desirable not only when the signal to noise ratio is poor, but also (as in the present case) when the spectrum consists of only one or a few main features or (as in the present case) when spectra are to be analyzed in terms of fitted models using only a few parameters (Ref. 17 contains a more complete discussion of these points).

B. Sample cell and experimental procedure

^{36}Ar has excellent neutron scattering properties but is a rare isotope and is not practical to work with in large quantities. It is therefore necessary

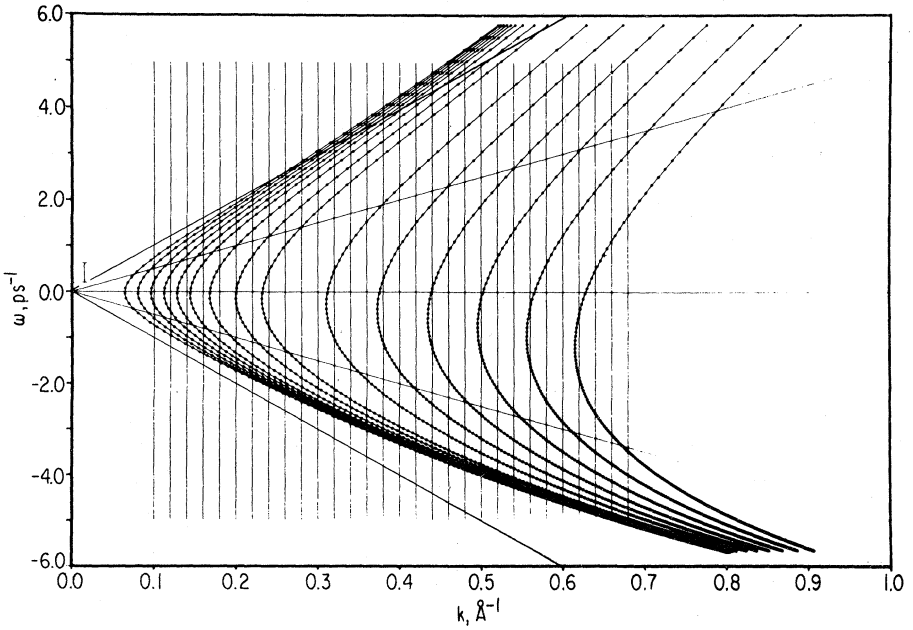

FIG. 3. The k-ω loci determined by the incident energy (4.84 meV) and scattering angles chosen for the present experiment. The error bar at the left is the FWHM of the spectrometer resolution function. The lines emanating from the origin show the dispersion of 500- and 1000-m/sec excitations.

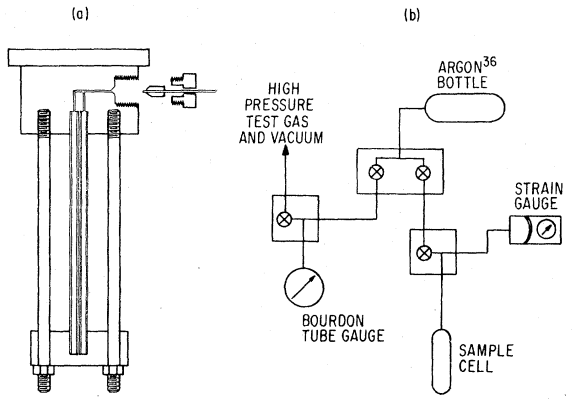

FIG. 4. High-pressure cell is shown in (a) and the gas-handling system schematically in (b). The valves enclosed in boxes are single units which contain either multiple inlets and/or multiple valve stems.

that the sample cell be cyclable in temperature, in order to condense the gas into it, that it have small dead volume in the noncycled external lines and pressure sensors, and that it be leak tight to 1%–2% changes in hundreds of atmospheres of pressure for periods of weeks as well as leak tight under short-term stresses of temperature cycling. In order to make the ratio of sample to container scattering favorable for reliable subtraction of the container signal from the sample signal, it is necessary that the container walls be as thin as possible. It is also desirable that as much sample be in the beam as is consistent with minimization of multiple-scattering effects.

The cell, gas handling system, and fittings are shown schematically in Fig. 4. The cell was designed and constructed by R. Kleb of Argonne engineering staff from 6061-T6 aluminum alloy. High-pressure lines were attached to the target by first hard-soldering stainless-steel capillary tubes of the type used in manufacturing hypodermic needles to cone shaped stainless-steel plugs which were then inserted into threaded glands. These glands were screwed into a threaded opening in the pressure cell so that the plug formed a metal to metal seal to the cell. The cell was fabricated from seamless 6061-T6 tubes of 0.48-cm o.d. and 0.071-cm wall thickness. The walls in the section of each tube illuminated by the neutron beam were machined down to a thickness of 0.05 cm and each tube was epoxied into insertion holes in the upper and lower support blocks. The walls at each end of the tubes were left at full thickness to minimize flexing the brittle epoxy seals, and each end of the tube and insertion hole was etched with acid to provide a rough surface for the epoxy. The two 0.64-cm diam. tie rods were added to reduce the axial stress on the tubes when they were pressurized. The tie rods were arranged so the high-pressure tubes could be elastically preloaded by hand-tightening nuts on the lower ends of the rods. All surfaces of the cell were masked from neutrons with Cd sheet so that only the thinned tube section was exposed to the incident beam through a 10 m × 0.64-cm slit. A string counter was used to check the uniformity of the beam intensity across its width and additional Cd shielding was used to minimize scattering from vacuum cans, beam windows, etc.

After careful checking of the cell and gas handling system for high-pressure micro-leaks, the ^{36}Ar sample was loaded by cooling the cell over a 6-h period to 83.8 °K while allowing ^{36}Ar to condense into the cell. The pressure in the sample bottle was monitored with a quartz Bourdon tube gauge in order to be certain that plugs were not being formed in the capillary tube. The cell was then sealed from the sample bottle and Bourdon tube and brought up to room temperature over a 5-h period. The pressure in the loaded cell was monitored throughout the experiment with a 0–30 000 psi strain-gauge transducer, which was chosen because of its small dead volume and flexibility for remote mounting. No average loss in pressure was observed during the two-week measurement period although the pressure was observed to fluctuate ±1.5 atm with changes in room temperature. At the end of the two-week period the argon was condensed back into the storage bottle and the cell was pressurized with 2.5-atm ^{3}He in order to experimentally measure container shielding effects. The efficiencies of the 15 detector groups and of the beam monitors were calibrated using a 1-mm slab of vanadium as a standard scatterer, the vanadium incoherent scattering cross section assumed to be 5.13 b.

IV. CORRECTIONS TO THE DATA

A. General considerations

The measured time-of-flight data were reduced to a fully corrected constant wave-vector-transfer representation of the scattering function $S(k, \omega)$ as described by Copley *et al.*[18] Briefly, the steps involved are removal of container scattering, conversion to $S(k, \omega)$, normalization via vanadium reference method, interpolation to constant k, evaluation of multiple-scattering effects, and correction for instrumental resolution. Several points of particular importance in the present case are discussed in detail below.

B. Container correction

In an actual neutron scattering measurement, the observed signal contains scattering from the

substance of interest (sample) and from the container which surrounds the sample. In practice, therefore, it is necessary to measure the signal from both filled and empty container in order to eliminate the container scattering. Since a neutron traversing either sample or container material has a finite probability of being scattered or absorbed, the scattering from the walls of the container is attenuated by the presence of material in it and the measured intensity from the empty container must be corrected for shielding before it is subtracted from the filled container signal.

Small-angle quasielastic scattering measurements are made particularly difficult by uncertainties associated with subtracting the resolution-broadened elastic container scattering from the quasielastic sample signal. In the present experiment, the (111) and (200) aluminum crystal planes Bragg scatter neutrons at 116° and 180° with respect to their incident direction. Many of these neutrons can in turn be Bragg scattered again into the forward direction. This results in intense scattering at small angles which varies strongly with the scattering angle. High-strength aluminum alloys are prepared by cold working and precipitation hardening. In consequence, the microscopic grain structure varies unpredictably from section to section of the same piece of alloyed material and so of course does the Bragg scattering. In order to minimize the magnitude of the necessary shielding correction to the empty data, scattering from the container was measured with 2.5 atm of ^{3}He in it. This simulated the removal of neutrons due to the presence of a sample medium in the container. In addition, the container scattered was measured as a function of ^{3}He pressure in order to estimate the importance of multiple Bragg processes. Adjustments to the self-shielding corrections were done using these data and the fully corrected "empty" container signal was subtracted from the filled container signal. Even with this care, analysis of the container subtraction indicates the presence of extreme shielding effects at the elastic position of the two smallest scattering angles of 2.4° and 3.0°. These shielding effects seem not to be explainable in

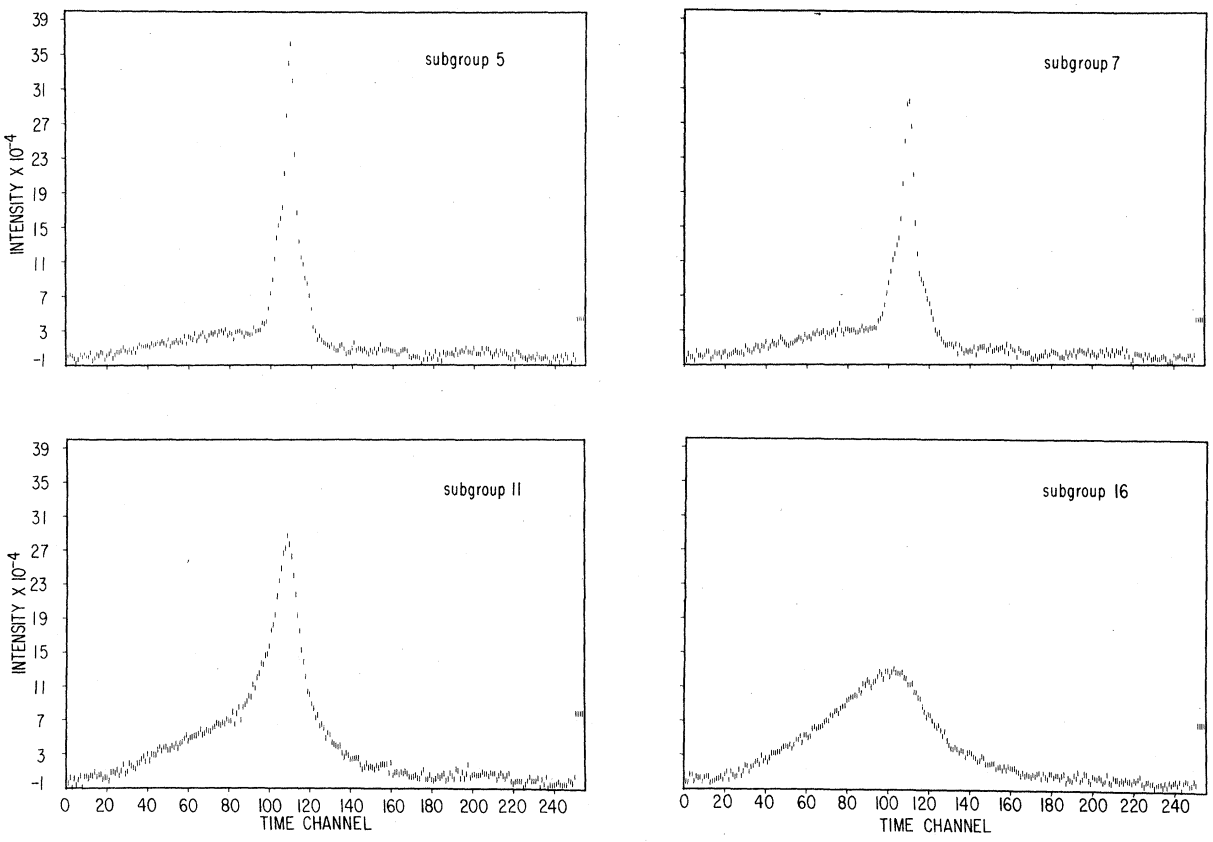

FIG. 5. Four typical examples of raw time-of-flight data after subtraction of empty container scattering. The scattering angles are 4.2° for (a), 5.4° for (b), 11.7° for (c), and 23.7° for (d). Note the extremely rapid change in the shape of the scattering law at the smaller angles.

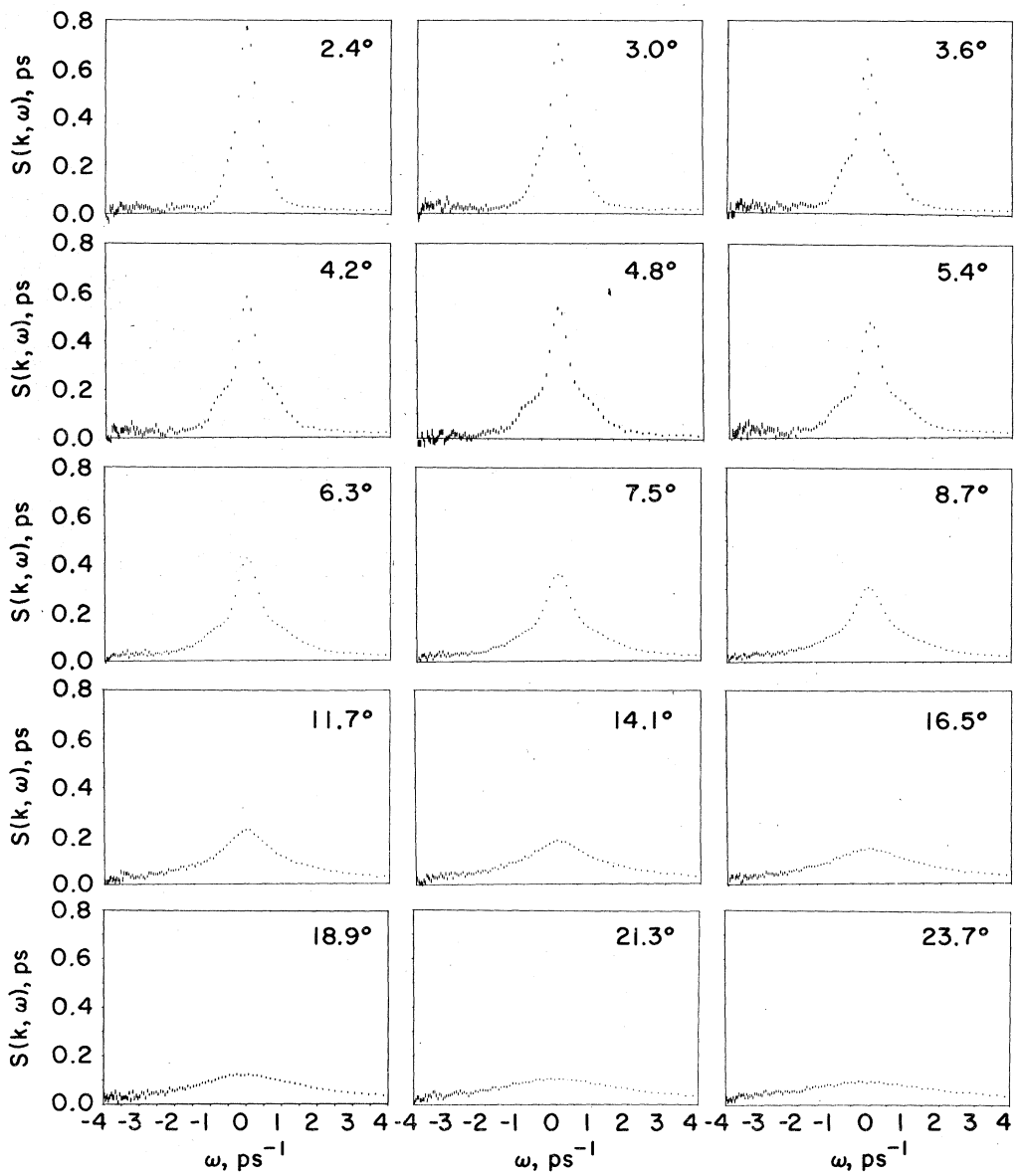

FIG. 6. Constant-angle dynamic structure factor as a function of neutron energy gain (expressed as angular frequency) for the 15 scattering angles studied. The overall uniformity of statistical errors is a feature of the correlation chopper technique and the tendency of the statistics to deteriorate from positive to negative frequencies is a result of transformation from time of flight to energy scales. Slight asymmetries in the data are seen at some scattering angles due to slightly different k-ω loci for upscattered and downscattered neutrons (see Fig. 3).

terms of multiple Bragg scattering. The elastic data from these scattering angles were therefore rejected because there was no reliable way to estimate further corrections from measurements or from sum rule arguments. The container correction was not severe at wave-vector transfers of 0.1 Å^{-1} or larger.

In Fig. 5 we show several typical time-of-flight spectra after removal of container scattering. Figure 6 shows our data converted to $S(k, \omega)$ at constant angle for all 15 scattering angles.

C. Multiple-scattering effects

The multiple-scattering correction was performed using the Monte Carlo computer code of Copley.[19] It was necessary to modify the code for a target in which two vertical tubes are partially illuminated by the incident neutron beam. The code was used to calculate single- and multiple-scattering events on a nonlinear grid of wave-vector transfers from 0.06 to 4.5 Å^{-1} and energy transfers from ±3meV around the 4.84-meV

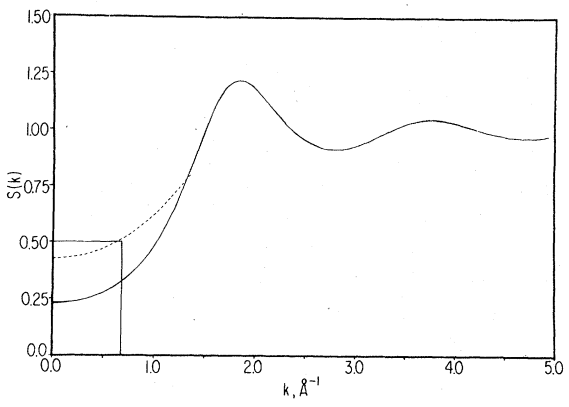

FIG. 7. Structure factor used in multiple-scattering calculations. The region of interest in the multiple-scattering correction is identified by the box in the lower left corner. Dashed curve, small-k estimate of structure factor used in calculation up to 1.4 $Å^{-1}$. Solid curve, Percus-Yevick prediction for $S(k)$ assuming 3.3-Å particles.

incident energy. The dynamic structure factor used in the multiple-scattering correction was calculated using the QTRT kinetic model and the structure factor above 1.4 $Å^{-1}$ was calculated using the Percus-Yevick hard-sphere structure factor.[20] Because the Percus-Yevick equations do not give the correct value of the structure factor at small k, the Percus-Yevick expressions were used with an artificially small packing fraction as an interpolation scheme to properly estimate the small-k behavior of the structure factor. The resulting structure factor is shown in Fig. 7. The results of the multiple scattering calculations for two typical angles are shown in Fig. 8. The multiple scattering is in all cases extremely broad and featureless. It should be noted that the calculated multiple-scattering correction is greater than the actual effect since the model structure factor goes to about 0.4 at $k=0$ instead of the thermodynamically determined value of 0.56. Our multiple-scattering calculation thus overestimates the ratio of multiple to single scattering by underestimating the structure factor at small k with respect to large k. In any case, it was not necessary to correct the measured data for multiple-scattering effects because the multiple scattering is broad, featureless, and small compared to first scattering.

D. Interpolation to constant k

The data were interpolated to a constant wave-vector-transfer representation by cubic spline interpolation. No effort was made to smooth the spline function because of the high statistical accuracy of the measured data. A three-dimensional representation of the resulting constant wave-vector-transfer scattering law is shown in Fig. 9.

The data of Fig. 9 are corrected for all experimental effects other than instrumental resolution, and it is this representation of the data with which theoretical models should be compared.[21] In order to obtain a representation of the dynamic structure factor of ^{36}Ar at 456 atm and 295 K free from resolution broadening, we have utilized a modeling procedure described below. In spite of the excellent fits to the data obtained, it must be recognized that questions of uniqueness of solutions and of building in of assumptions always

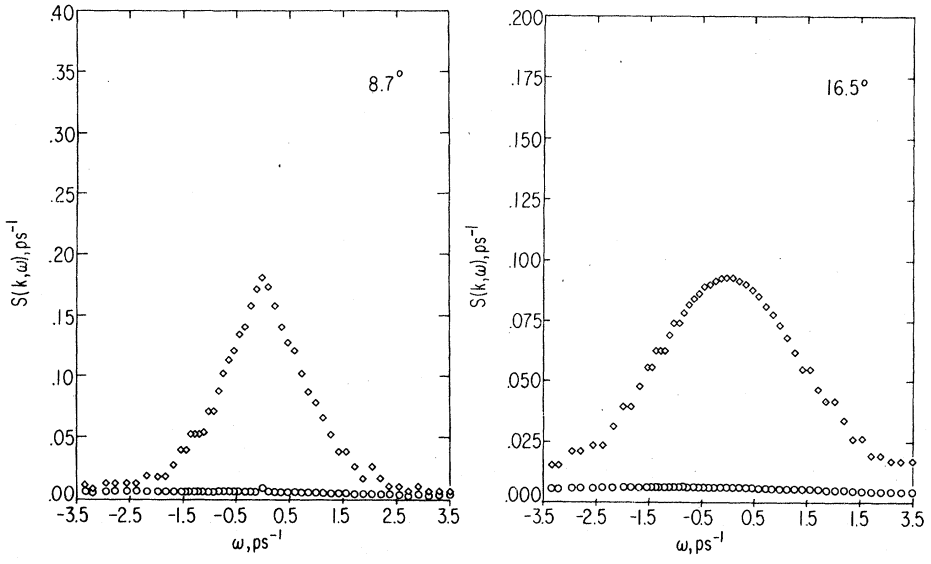

FIG. 8. Estimates of multiple-scattering effects in our data for two typical scattering angles. Squares, single scattering; circles, multiple scattering; crosses, total.

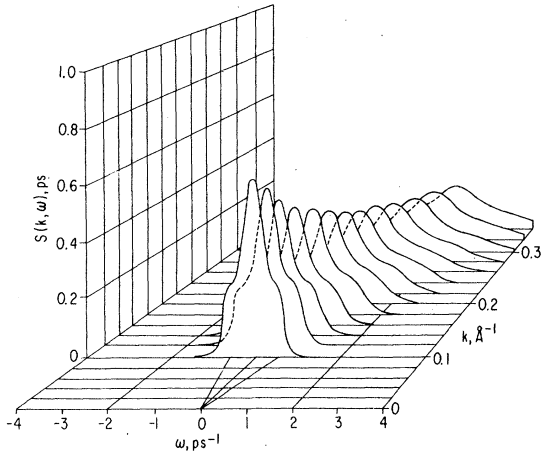

FIG. 9. Dynamic structure factor, corrected for all effects except instrumental resolution. The importance of resolution effects in the data can be assessed by comparing this representation with Fig. 11.

remain in any fitting procedure, and for this reason Fig. 9 should be considered the most reliable representation of our experimental results.

E. Resolution correction

A measurement of the symmetrized scattering function $S_m(\vec{k}, \omega)$ yields in general a convolution of the true dynamic structure factor $S_t(\vec{k}, \omega)$ with the normalized resolution function of the spectrometer,

$$S_m(\vec{k}, \omega) = \int d\vec{k}' \int d\omega' R(\vec{k}, \vec{k}', \omega, \omega') S_t(\vec{k}', \omega') .$$

The resolution of a hybrid time-of-flight spectrometer as used in this experiment has contributions which are constant in time-of-flight, constant in energy transfer, and variable in wave vector and energy transfer. Although it is usually argued, by invoking the central limit theorem, that

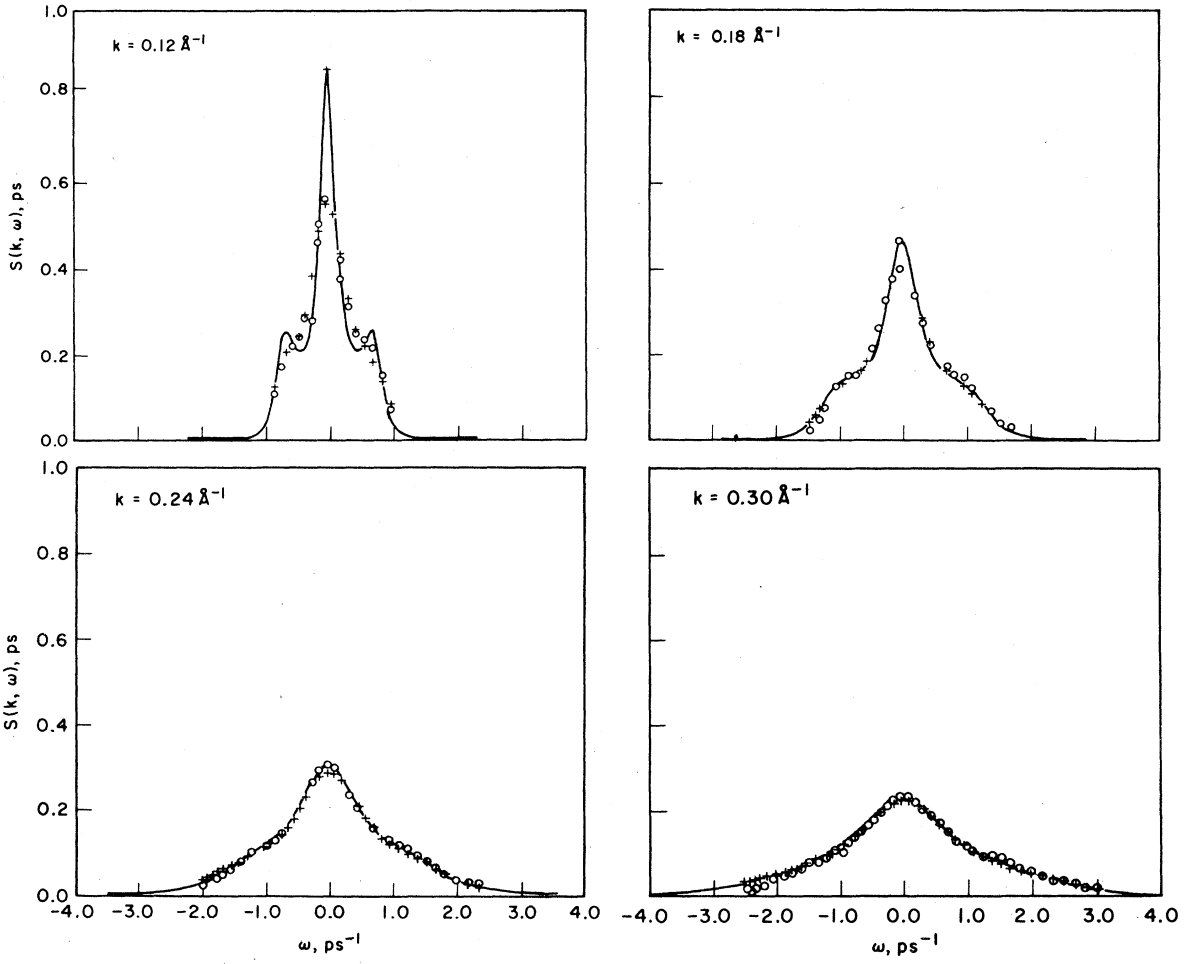

FIG. 10. Four typical kinetic-model fits to the measured data at different fixed values of the wave-vector transfer. Circles, measured data points; crosses, resolution-broadened kinetic-model fits; solid curve, best fit to the measured spectra for fixed $r_0 = 3.4$ Å. The quality of fit as measured by χ^2 is summarized in Table II. The fitted parameters $g(r_0)$ and $S(k)$ are plotted vs wave vector in Figs. 12(a) and 12(b).

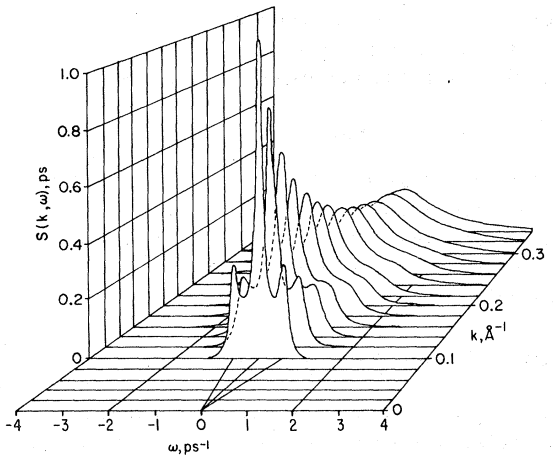

FIG. 11. Fully corrected dynamic structure factor: kinetic model fit to neutron data with fixed $r_0 = 3.4$ Å, $g(r_0)$ and $S(k)$ allowed to vary (see text).

the resolution function tends to a Gaussian shape, there are in fact significant non-Gaussian corrections to the shape. These effects can be quite severe at small wave-vector and energy transfers where the k dependence of the scattering law is strong. Attempts to test model scattering laws against resolution-affected data using simplified versions of the resolution function should be carefully checked for consistency.

The resolution function used to test model scattering functions in the present case was derived from the measured symmetrized vanadium $S(k, \omega)$. It was assumed that the resolution has no explicit dependence on wave-vector transfer. Furthermore, the resolution width was assumed to be constant in time of flight rather than energy. The consistency of these assumptions was examined by fitting the triple relaxation kinetic model[13] to constant wave-vector-transfer data for the vanadium-derived resolution function and for Gaussian functions with widths constant in both time and energy. All fits led to essentially the same kinetic-model parameters. The best fit, as measured by the least-squares sum, was obtained for the vanadium-derived function. The worst fit was obtained for the Gaussian function with width constant in energy transfer. In addition, the combined consistency of the data and the resolution assumptions were tested by performing fits to only the neutron energy gain or loss portion of the measured spectra. The fit to energy gain data alone resulted in a collective excitation at 0.1 $Å^{-1}$ with a speed of 580 m/sec, the fit to energy-loss data alone resulted in a 570-m/sec excitation speed, and the fit to the entire spectrum resulted in a propagation speed of 570 m/sec. Differences in the intensity at the position of the collective

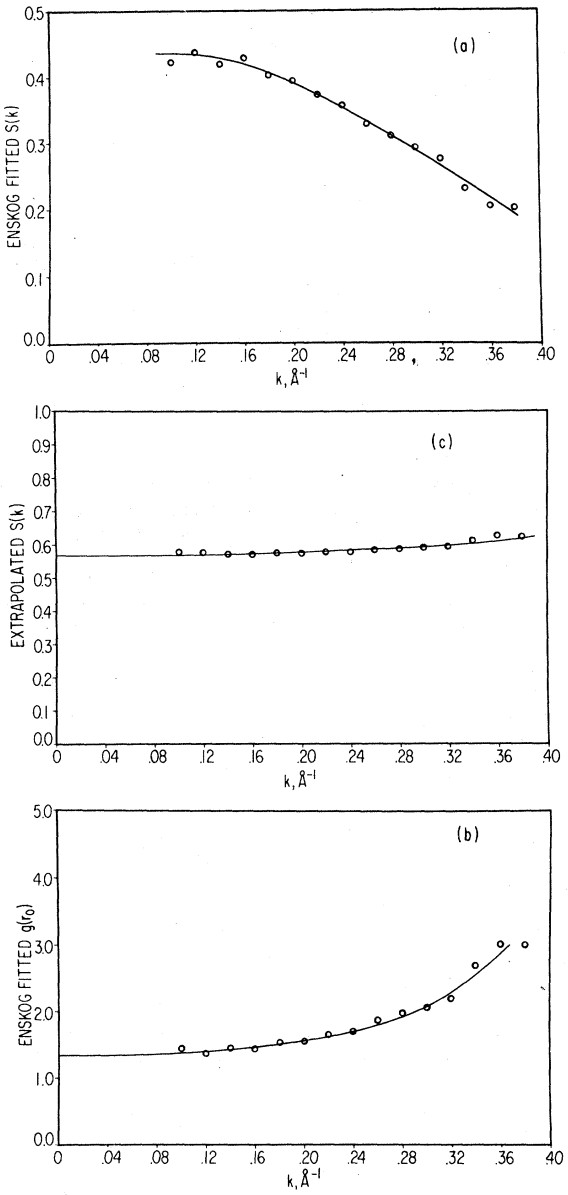

FIG. 12. (a) Kinetic-model structure factor $S(k)$. (b) Pair correlation function at contact $g(r_0)$ arrived at by fixing hard-sphere diameter $r_0 = 3.4$ Å and fitting for a minimum value of χ^2 at each wave vector. (c) True structure factor (related to intensity rather than as a kinetic equation shape parameter) arrived at using best fits to data to estimate the scattering law at energy transfers not reached by our measurement.

mode for the separate fits to energy-gain and loss data differed by about 5%. The fit to the full spectrum resulted in an intensity at the collective mode position which was consistent with the partial fits. Some typical fits to the data are shown in Fig. 10 for the case where the hard-sphere

diameter r_0 has been fixed at 3.4 Å and $S(k)$ and $g(r_0)$ have been treated as fitting parameters. The slight asymmetry in the smaller-k data is due to the strong k dependence of the scattering law at the smallest wave-vector transfers.

At these small angles, the positive and negative frequencies tend to be averaged differently by the true four-dimensional resolution of the spectrometer. There are additional contributions to this asymmetry from the neglected k and ω dependence of the resolution function. It is known, however, that these errors are to a large extent equal and opposite for positive and negative frequencies,[22] and as described above do not appear to importantly influence the fitting results. However, conclusions drawn from the smallest-k data must still be viewed with caution. Nevertheless, we present below some interesting results arrived at from different kinetic-model fits to these data. In Fig. 11 we show a three-dimensional plot of the resolution-corrected dynamic structure factor arrived at by fixing the hard-sphere diameter at $r_0 = 3.4$ Å and treating $S(k)$ and $g(r_0)$ as fitting parameters. This plot shows the qualitative features of the true power spectrum of thermally excited density fluctuations as measured by thermal neutron scattering.

V. RESULTS AND DISCUSSION

The validity of the generalized Enskog equation was carefully examined by computing the dynamic structure factor using the QTRT kinetic model to numerically calculate the power spectrum of thermally excited density fluctuations for the set of parameters r_0, $g(r_0)$, and $S(k)$. The kinetic-model spectra were then normalized to the intensity of the measured data, folded with the spectrometer resolution, and compared to the measured data. The procedure was performed by fixing the value of r_0 and allowing $S(k)$ and $g(r_0)$ to vary until the quantity χ^2 defined as

$$\chi^2 = \frac{1}{N-f+1} \sum_{i=1}^{N} \left(\frac{S_i^{\text{exp}} - S_i^{\text{theory}}}{\Delta S_i^{\text{exp}}} \right)^2 ,$$

was minimized. Here S_i^{exp} is the i^{th} element of the measured dynamic structure factor, S_i^{theory} the i^{th} element of the resolution-broadened model dynamic structure factor, ΔS_i^{exp} the statistical uncertainty in S_i^{exp}, N the number of data points, and f the number of fitting parameters. The data at each fixed value of the wave-vector transfer were fitted independently.

A value $r_0 = 3.4$ Å was initially chosen and values of $g(r_0)$ and $S(k)$ were arrived at by fitting for the

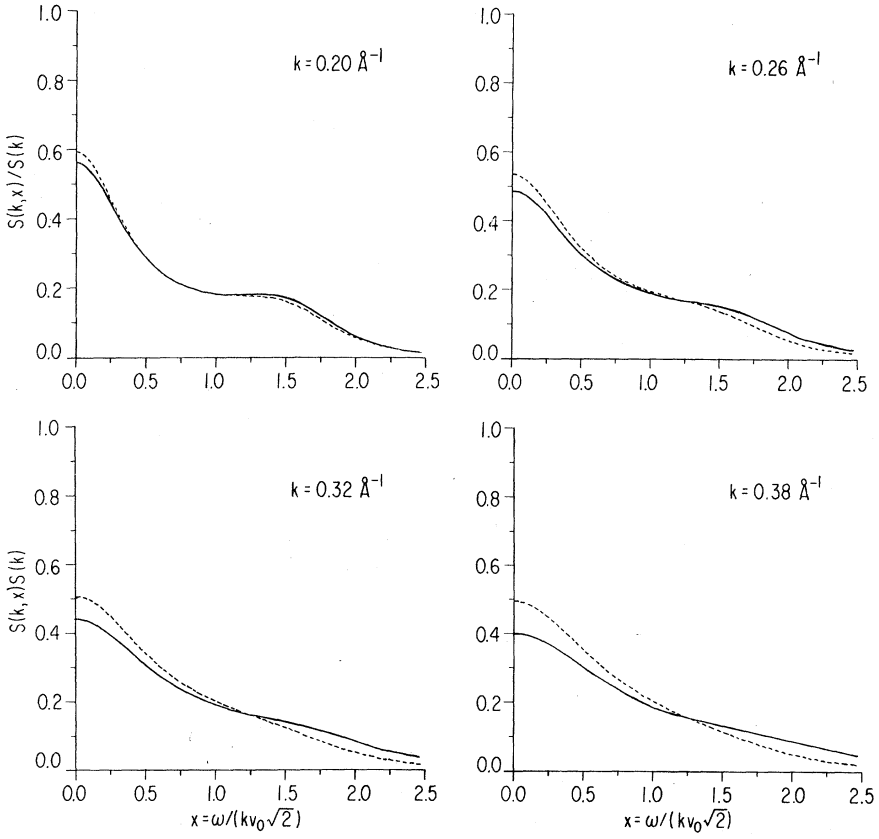

FIG. 13. Effect on the qualitative shape of the power spectrum for k-dependent structure factor $S(k)$ and pair correlation at contact $g(r_0)$. Hard-sphere diameter fixed at $r_0 = 3.4$ Å. Dashed curve, prediction of Enskog theory using parameters derived from best fit to the $k = 0.10$-Å^{-1} data. Solid curves, best fits to data at each k obtained by fitting values of $g(r_0)$ and $S(k)$ which minimize χ^2 for $r_0 = 3.4$ Å.

TABLE II. Values of χ^2 (defined in text) for fits to neutron spectra with $r_0 = 2.6$ and 3.4 Å, $g(r_0)$, and $S(k)$ used as fitting parameters.

k (Å^{-1})	$\chi^2(r_0 = 2.6$ Å)	$\chi^2(r_0 = 3.4$ Å)
0.10	4.863	5.005
0.12	4.084	5.094
0.14	3.915	4.784
0.16	4.007	3.863
0.18	3.443	4.072
0.20	3.958	5.014
0.22	3.797	5.445
0.24	3.687	4.992
0.26	3.445	4.882
0.28	3.486	4.501
0.30	3.536	4.063
0.32	3.125	3.699
0.34	2.951	3.561
0.36	2.498	2.943
0.38	2.284	2.631

minimum χ^2 from 0.10 to 0.38 Å^{-1} at increments of 0.02 Å^{-1} (see Fig. 3). The fits at 0.10, 0.12, 0.14, and 0.16 Å^{-1} resulted in values of $g(r_0)$ and $S(k)$ which were constant within estimated uncertainties of the measuring procedure. Above 0.18 Å^{-1} the values of $g(r_0)$ were found to increase monotonically and the values of $S(k)$ to decrease monotonically. The k dependence of these parameters for r_0 fixed at 3.4 Å is shown in Fig. 12. The extreme flatness of the structure factor at these wave vectors contradicts initial results of a computer experiment presently in progress in our group.[23] The reason for the discrepancy is as yet unresolved. The absolute value of the structure factor at $k = 0$ determined from classical compressibility measurements is $S(0) = 0.56$. The estimate obtained from our neutron scattering measurement is 0.58 ± 0.01. Figure 13 shows the effect of the k-dependent parameters on the shape of the QTRT power spectrum. The dashed curves show the shape of the normalized spectrum when $k = 0.10$-Å^{-1} kinetic-model parameters are used to calculate the line shape at $k = 0.20$, 0.26, 0.32, and 0.38 Å^{-1}. The solid curves are the spectra found by least-squares fitting the kinetic-model parameters to the data. The $k = 0.10$ Å^{-1} parameters reproduce almost perfectly spectra at 0.20 Å^{-1} although the $k = 0.20$-Å^{-1} model parameters differ from the $k = 0.10$-Å^{-1} values by about 5%. This indicates that the dependence of the power spectrum predicted by the generalized Enskog equation is qualitatively correct. At $k = 0.26$, 0.32, and 0.38 Å^{-1} the best-fit spectral shapes become in-

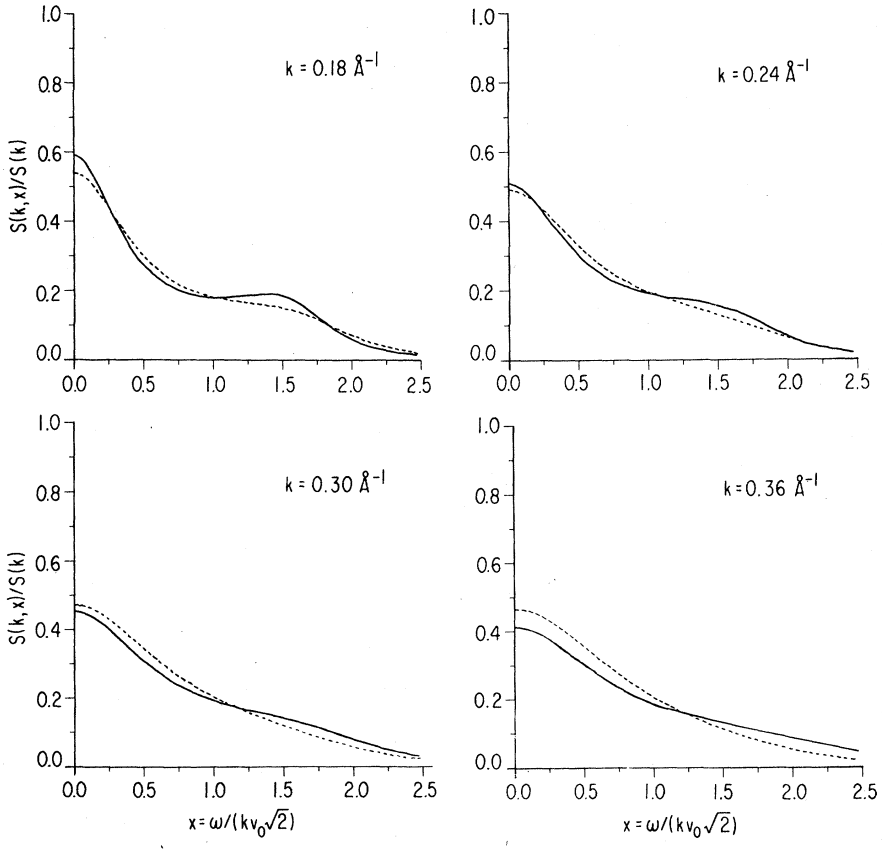

FIG. 14. Differences in shape of the power spectrum for best fits to data with $r_0 = 3.4$ and 2.6 Å. Solid curve, best fit for $r_0 = 2.6$ Å; dashed curve, best fit for $r_0 = 3.4$ Å. The $r_0 = 2.6$-Å fits are significantly better at all wave vectors except one. Values of χ^2 are summarized in Table II.

creasingly different from the spectral shapes generated using the $k = 0.10\text{-Å}^{-1}$ Enskog parameters. The differences in the spectral shapes indicate a "stiffer" response function at the higher wave-vector transfers.

The Enskog theory was also tested by fitting with progressively smaller values of the hard-sphere diameter. The fit to the data was found to improve at all but one value of wave-vector transfer until a hard-sphere diameter of 2.6 Å was reached. Table II shows the value of χ^2 for k-independent fits to the data with r_0 fixed at 3.4 and 2.6 Å. The spectral shapes for 3.4- and 2.6-Å particles are shown in Fig. 13. The full curves are the spectral shapes for 2.6-Å particles and the dashed curves for 3.4-Å particles.

The shapes of our best estimate of the dynamic structure factor of argon gas at 456 atm and 295 K are compared with the power spectra predicted by the Enskog theory using parameters derived from the best fit to the $k = 0.10\text{-Å}^{-1}$ data for two values of r_0 in Fig. 14. The solid curves are those obtained from the best fits using 2.6-Å particles and the dashed curves are the best fits using 3.4-Å particles. The qualitative differences indicate that the high-temperature gas exhibits greater structure in the power spectrum than the Enskog theory is capable of producing. In Fig. 15 we show a qualitative comparison of the actual k dependence of the spectral shape and the k dependence predicted from the $k = 0.10\text{-Å}^{-1}$, $r_0 = 3.4$-Å fit.

In Table III, the calculated thermal conductivity and shear viscosity of argon at 456 atm and 295 K for best fits with different hard-sphere diameters are shown. The transport coefficients were arrived at by averaging the fitted values of $g(r_0)$ from the four smallest wave vectors and using the QTRT expressions for the transport coefficients. The transport coefficients as measured by classical techniques[5] are listed for comparison. Note that the thermal conductivity and viscosity must be scaled by $\alpha = (39.948/35.968)^{1/2}$ and α^{-1}, respectively, in order to correct for the isotopic

TABLE III. Comparison of classically measured transport coefficients with those derived from Enskog equation fits to neutron data.

Bulk transport coefficients

Speed of sound:	$C_0^{\text{nat}} = 541$ m sec^{-1}
	$C_0^{36} = 570$ m sec^{-1}
Shear viscosity:	$\eta_s^{\text{nat}} = 4.64\times10^{-4}$ g cm^{-1} sec^{-1}
	$\eta_s^{36} = 4.89\times10^{-4}$ g cm^{-1} sec^{-1}
Thermal conductivity:	$\lambda^{\text{nat}} = 4.41\times10^{3}$ erg cm^{-1} sec^{-1} K^{-1}
	$\lambda^{36} = 4.65\times10^{3}$ erg cm^{-1} sec^{-1} K^{-1}

QTRT transport coefficients

$$\lambda = \lambda_0[\,1/g(r_0) + 4.8f + 12.2784f^2 g(r_0)]$$
$$\eta = \eta_{s0}[1/g(r_0) + 3.2f + 12.336f^2 g(r_0)]$$
$$c_0 = v_0\{1 - nC(0) + \tfrac{2}{3}[1 + 4fg(r_0)]^2\}^{1/2}$$

where

$$\lambda_0 = 75k_B v_0/64 r_0^2\sqrt{\pi}$$
$$\eta_{s0} = 5mv_0/16 r_0^2\sqrt{\pi}$$
$$v_0^2 = k_B T/m \text{ (thermal velocity)}$$
$$f = n\pi r_0^3/6 \text{ (packing fraction)}$$

Values of transport coefficients for different fits

r_0	$g(r_0)$	η_s (10^{-4} g cm^{-1} sec^{-1})	λ (10^3 erg cm^{-1} sec^{-1} K^{-1})
3.4	1.426	5.022	4.992
3.3	1.550	4.874	4.845
3.2	1.650	4.725	4.697
3.1	1.794	4.578	4.551
3.05	1.866	4.505	4.478
3.0	1.945	4.432	4.406
2.9	2.121	4.286	4.260
2.8	2.318	4.141	4.116
2.7	2.542	3.996	3.972
2.6	2.798	3.853	3.829
2.5	3.092	3.709	3.686

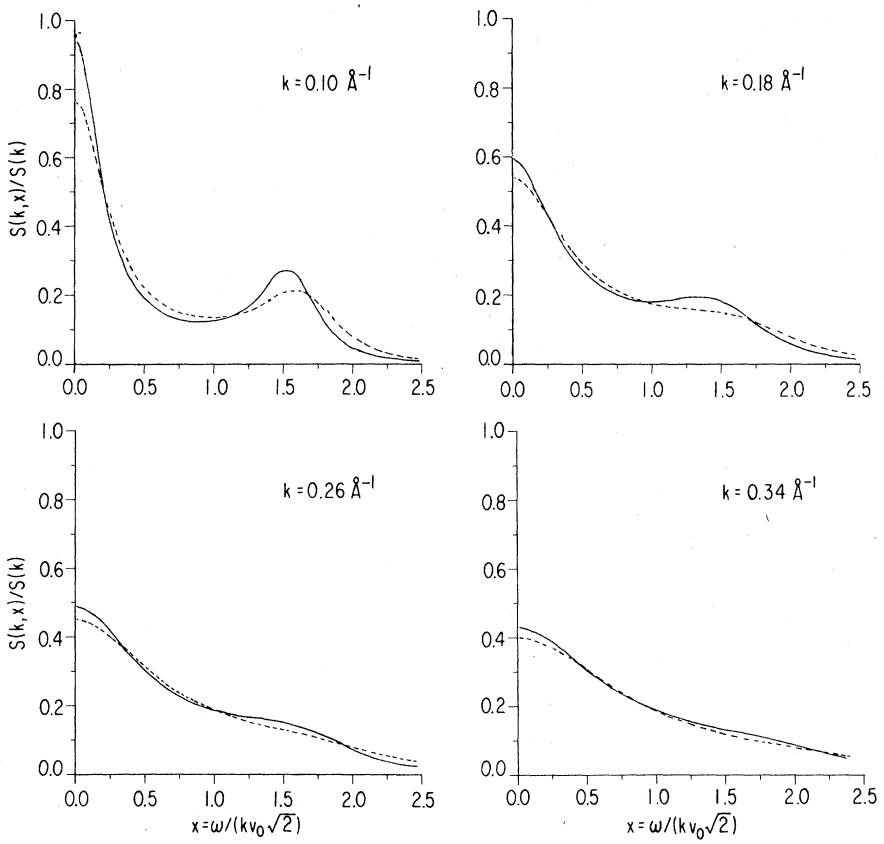

FIG. 15. Best fits for 2.6-Å particles compared to predictions of the generalized Enskog equation. Solid curves, best fits to data with $r_0 = 2.6$ Å; dashed curves, predictions using $r_0 = 3.4$ Å and the $S(k)$ and $g(r_0)$ obtained from best fit to $k = 0.10$-Å^{-1} data.

mass difference between natural argon and ^{36}Ar. The QTRT fit using $r_0 = 3.3$ Å provides the best overall agreement with the mass-scaled measured transport coefficients. The thermal conductivity estimated from the neutron spectra for fits using $r_0 = 3.3$ Å is some 4% higher than the scaled transport coefficient while the shear viscosities are essentially in perfect agreement. The fits using $r_0 = 3.2$ Å agree within 3% for the shear viscosity and within 1% for the thermal conductivity. The position of the sound peak at 0.10 Å^{-1} indicates a sound velocity of 570 ± 20 m/sec and the ratio of the specific heats C_p/C_v estimated using the fitted small-k Enskog parameters and evaluating them at $k = 0$ is 2.35 ± 0.05. The measured specific-heat ratio is $C_p/C_v = 2.51$. The small-k Enskog parameter estimates of the transport and thermodynamic properties of the system are thus substantially consistent with those measured by classical procedures.

VI. SUMMARY

We have measured the power spectrum of thermally excited density fluctuations of the high-temperature dense gas ^{36}Ar. We find substantial consistency with some qualitative features of the generalized Enskog description although quantitative differences remain. The present measurement is a demonstration of the potential offered by neutron scattering techniques for measuring the dynamic structure of simple fluids sufficiently precisely to allow quantitative tests of theories in the hydrodynamic-to-kinetic transition regime.

It should be noted that there exists a wide class of simple systems the thermodynamic, transport, and neutron scattering properties of which are closely related to those of monatomic fluids. Such systems as binary monatomic mixtures and diatomic fluids offer the possibility of carefully and systematically identifying discrepancies in the dynamical behavior of reasonably similar simple systems. Combining these measurements with computer molecular dynamics studies should hopefully provide a more complete picture of simple fluids, which must ultimately form the basis of our knowledge of the liquid state.

We gratefully acknowledge the substantial encouragement, support, and contributions this work has received from A. Rahman and G. F. Mazenko as well as the ingenuity and technical assistance of R. Kleb and G. Ostrowski. This work was performed under the auspices of the U. S. Department of Energy.

[1]N. A. Clark, Phys. Rev. A 12, 232 (1975); H. Bell, H. Moeller-Wenghoffer, A. Kollmar, R. Stockmeyer, T. Springer, and H. Stiller, Phys. Rev. A 11, 316 (1975); K. Carneiro and J. P. McTague, Phys. Rev. A 11, 1744 (1975).

[2]B. J. Berne and D. Forster, Ann. Rev. Phys. Chem. 22, 563 (1971).

[3]R. D. Mountain, in *Dynamics of Solids and Liquids by Neutron Scattering*, edited by S. W. Lovesey and T. Springer (Springer-Verlag, Berlin, 1977). (See also Refs. 8 and 9.)

[4]A. Rahman, Phys. Rev. 136, A405 (1964); D. Levesque, L. Verlet, and J. Kürkijarvi, Phys. Rev. A 7, 1690 (1973), and references contained therein.

[5]H. J. M. Hanley and E. G. D. Cohen, Physica 83, 215 (1976); H. J. M. Hanley, R. D. McCarty, and E. G. D. Cohen, Physica 60, 322 (1971). J. V. Sengers, Int. J. Heat Transfer 8, 1103 (1965), and *Recent Advances in Engineering Science, Vol. III*, edited by A. C. Eringen (Gordon and Breach, New York, 1968), p. 153.

[6]B. J. Alder, W. E. Alley, and S. Yip (private communication).

[7]L. Van Hove, Phys. Rev. 95, 249 (1954).

[8]J. P. Hansen and I. R. McDonald, *Theory of Simple Liquids* (Academic, New York, 1976); P. A. Egelstaff, *An Introduction to the Liquid State* (Academic, New York, 1967).

[9]See reviews, in *Statistical Mechanics, Part B*, edited by B. J. Berne (Plenum, New York, 1977); J. R. Dorfman and H. van Beijeren, *ibid.* p. 65 and G. F. Mazenko and S. Yip, *ibid.* p. 181; P. M. V. Resibois, *Classical Kinetic Theory of Fluids* (Wiley, New York, 1977).

[10]G. F. Mazenko, T. Y. C. Wei, and S. Yip, Phys. Rev. A 6, 1981 (1972); M. S. Jhon and D. Forster, Phys. Rev. A 12, 254 (1975); J. J. Duderstadt and A. Z. Akcasu, Phys. Rev. A 1, 905 (1970); 2, 1097 (1970).

[11]J. L. Lebowitz, J. K. Percus, and J. Sykes, Phys. Rev. 188, 487 (1967); H. H. U. Konijnendijk and J. M. J. Van Leuween, Physica 64, 342 (1973); H. Van Beijeren and M. H. Ernst, Physica 68, 437 (1973); A. Z. Akcasu, Phys. Rev. A 7, 182 (1973); G. F. Mazenko, Phys. Rev. A 9, 360 (1974).

[12]P. M. Furtado, G. F. Mazenko, and S. Yip, Phys. Rev. A 12, 1653 (1975).

[13]P. M. Furtado, G. F. Mazenko, and S. Yip, Phys. Rev. A 13, 1641 (1976).

[14]D. Forster and P. C. Martin, Phys. Rev. A 2, 1575 (1970); D. Forster, Phys. Rev. A 9, 943 (1974); G. F. Mazenko, Phys. Rev. A 9, 360 (1974).

[15]R. Kleb, G. E. Ostrowski, D. L. Price, and J. M. Rowe, Nucl. Instrum. Methods 106, 221 (1973).

[16]K. Sköld, Nucl. Instrum. Methods 63, 114 (1968).

[17]D. L. Price and K. Sköld, Nucl. Instrum. Methods 82, 208 (1970).

[18]J. R. D. Copley, D. L. Price, and J. M. Rowe, Nucl. Instrum. Methods 107, 501 (1973).

[19]J. R. D. Copley, Comput. Phys. Commun. 7, 289 (1974); 9, 59 (1975); 9, 64 (1975).

[20]N. W. Ashcroft and J. Lekner, Phys. Rev. 145, 83 (1966); M. S. Wertheim, Phys. Rev. Lett. 10, 321 (1963); E. Thiele, J. Chem. Phys. 39, 474 (1963).

[21]Tables of the fully corrected $S(k,\omega)$ as shown in Fig. 9 and of the modeled $S(k,\omega)$ shown in Fig. 11 are available from the authors.

[22]D. L. Price (unpublished).

[23]T. A. Postol, C. A. Pelizzari, and A. Rahman (unpublished).